Atmos. Meas. Tech. Discuss., doi:10.5194/amt-2016-48, 2016
Manuscript under review for journal Atmos. Meas. Tech.
Published: 6 April 2016

Atmospheric Measurement Techniques
Discussions

Improvements of the OMI O_2-O_2 Operational Cloud Algorithm and Comparisons with Ground-Based Radar-Lidar Observations

J. Pepijn Veefkind[1,2], Johan F. de Haan[1], Maarten Sneep[1], Pieternel F. Levelt[1,2]

[1]Royal Netherlands Meteorological Institute (KNMI), De Bilt, The Netherlands
[2]Delft University of Technology, Faculty of Civil Engineering and Geosciences, Delft, The Netherlands

Abstract. The OMI (Ozone Monitoring Instrument) OMCLDO2 cloud product supports trace gas retrievals of for example ozone and nitrogen dioxide. The OMCLDO2 algorithm derives the effective cloud fraction and effective cloud pressure using a DOAS fit of the O_2-O_2 absorption feature around 477 nm. A new version of the OMI OMCLDO2 cloud product is presented that contains several improvements, of which the introduction of a temperature correction on the O_2-O_2 slant columns and the updated look-up-tables have the largest impact. Whereas the differences in the cloud fraction are limited to approximately 0.1, the differences of the cloud pressure can be up to 200 hPa, especially at cloud fractions below 0.3. As expected, the temperature correction depends on latitude and season. The updated look-up tables have a systematic effect on the cloud pressure at low cloud fractions. The improvements at low cloud fractions are very important for the retrieval of trace gases in the lower troposphere, for example for nitrogen dioxide and formaldehyde. The cloud pressure retrievals of the improved algorithm are compared with ground-based radar-lidar observations for three sites in the mid-latitudes. For low clouds that have a limited vertical extent the comparison is favorable. For higher clouds, which are vertically extensive and often contain several layers, the satellite retrievals give a lower cloud-height. For high clouds mixed results are obtained.

Introduction

The Ozone Monitoring Instrument (OMI) is a imaging spectrometer developed by The Netherlands and Finland that has been launched in 2004 on board of the NASA EOS Aura satellite (Levelt et al., 2006). OMI has a continuous spectral coverage from 270-500 nm, with a resolution of approximately 0.5 nm. The primary data products from OMI are concentrations of trace gases, including ozone, nitrogen dioxide and formaldehyde. The trace gas retrieval algorithms rely on a priori information of cloud properties. For tropospheric trace gas retrievals, clouds are among the leading error sources in the retrieval (e.g. Boersma et al., 2011).

The OMI O_2-O_2 cloud product (OMCLDO2) contains information on the cloud fraction and cloud pressure for each ground pixel. The OMCLDO2 product has been designed to support the trace gas retrieval algorithms and is therefore driven by what these algorithms need for cloud information. The trace gas retrieval algorithms use the independent pixel approximation (Zuidema and Evans, 1998) representing clouds as Lambertian reflectors with a fixed albedo of 0.8 (Stammes et al., 2008). To be consistent with the trace gas retrievals, the OMCLDO2 product uses the same cloud model. The initial OMCLDO2 algorithm has been described by Acarreta et al. (2004). Because the amount of information

Atmos. Meas. Tech. Discuss., doi:10.5194/amt-2016-48, 2016
Manuscript under review for journal Atmos. Meas. Tech.
Published: 6 April 2016

Atmospheric Measurement Techniques Discussions
Open Access

in the OMI spectral range is limited, the algorithm derives an effective cloud fraction and an effective cloud pressure. The cloud fraction and cloud pressure are derived from the continuum radiance and the depth of the O_2-O_2 absorption feature around 477 nm. The algorithm does not distinguish between clouds and aerosols. Cloud-free conditions with significant thick aerosols layers will be represented by small cloud fractions. Similarly, thin clouds, for instance cirrus, will also be represented by a small cloud fraction. The main a-priori information that is used is the surface reflectance and the surface altitude, which are obtained from static look-up tables. Validation studies (Sneep et al., 2008) have shown that the effective cloud fraction compares well with effective cloud fractions derived from the cloud optical thickness observed by MODIS (Moderate Resolution Imaging Spectroradiometer) and that the derived cloud pressure determines a level somewhere near the middle of the clouds. This is different from the cloud pressures derived from the thermal infrared, which are very sensitive near the actual cloud tops. The OMCLDO2 retrieval is very similar to the FRESCO algorithm (Wang et al., 2008) with the difference that it is based on O_2-O_2 rather than O_2 absorption lines. The reason for using O_2-O_2 is that the OMI spectral range doesn't cover the oxygen absorption bands. An important difference of using the oxygen dimer is that its absorption scales with the oxygen density squared, which makes it increasingly more sensitive to the lower altitudes in the atmosphere. Besides the OMCLDO2 algorithm, there is also an OMI product based on the information from Raman scattering (Joiner et al., 2012; Joiner and Vassilkov, 2006). It has been demonstrated that this product is also sensitive to the middle of cloud layers, which has been referred to as the optical centroid pressure.

This paper describes version 2.0 of the OMCLDO2 product. Whereas updates and reprocessing was performed regularly in the past, the version 2.0 contains the following improvements and extensions:

1. A temperature correction is implemented which is needed because of the density-squared nature of the O_2-O_2 absorption;
2. Besides the independent pixel approximation, a second cloud model is implemented, which represents the scene as a Lambertian surface at a certain pressure level. The retrieved parameters are the scene albedo and scene pressure;
3. The look-up-tables that are used to derive the cloud fraction and pressure have a higher number of nodes, especially for the surface albedo and the surface altitude;
4. A method has been implemented to remove outliers from the spectral fitting;
5. The resolution of the a priori surface altitude is brought in line with the average OMI spatial resolution;
6. The gas absorption cross-sections are made consistent with the OMI NO_2 retrieval algorithm (Geffen et al., 2014).

This paper is organized as follows: in section 2 we describe the OMCLDO2 algorithm, focusing on the improvements that have been introduced in this version. In section 3 we discuss differences compared to the previous version. In section 4 we present comparisons of the cloud pressure to ground based radar observations.

Atmos. Meas. Tech. Discuss., doi:10.5194/amt-2016-48, 2016
Manuscript under review for journal Atmos. Meas. Tech.
Published: 6 April 2016

Atmospheric Measurement Techniques Discussions

Algorithm

The OMCLDO2 retrieval consists of two main steps: first a DOAS (Differential Absorption Spectroscopty) fit is performed on the spectral region between 460 and 490 nm to derive the O_2-O_2 slant column amount $N_{s,O2\text{-}O2}$ and the continuum reflectance R_c. In the second step these parameters are converted into cloud fraction c_f, cloud pressure p_{cld}, scene albedo A_{scn} and scene pressure p_{scn}.

DOAS fit

The DOAS fit is performed on the Earth's reflectance. OMI measures the Earth's radiance and once per day the solar irradiance. The wavelength grids of the Earth radiance and solar irradiance differ, because of the Doppler shift and because of non-homogeneous filling of the slit for partly cloudy scenes (Voors et al., 2006). For each ground pixel, the radiance (I) and irradiance (F) are brought on the same spectral grid (see Van Geffen et al., 2015) and the reflectance is calculated as $R(\lambda) = \frac{\pi\, I(\lambda)}{\cos\theta_0\, F(\lambda)}$, where λ is the wavelength and θ_0 is the solar zenith angle. Next, the following equation is used for the DOAS fit:

$$R(\lambda) = P(\lambda) e^{-(N_{s,O2O2}\sigma_{O2O2}(\lambda)+N_{s,O3}\sigma_{O3}(\lambda))} \cdot (1 + c_R \frac{I_R(\lambda)}{F(\lambda)}) \qquad (1)$$

where $P(\lambda)$ a polynomial of the first order, $N_{s,O2O2}$ the slant column of O_2-O_2, $\sigma_{O2O2}(\lambda)$ the O_2-O_2 cross section convolved with the OMI slit function, $N_{s,O3}$ the slant column of O_3, $\sigma_{O3}(\lambda)$ the O_3 cross section convolved with the OMI slit function, $I_R(\lambda)$ a synthetic radiance Raman spectrum convolved with the OMI slit function and c_R a scale parameter for the amount of Raman scattering. For the reference cross sections for O_2-O_2 we use (Thalman and Volkamer, 2013) at 293 K and for O_3 we use (Bogumil et al., 2000) at 220 K.

We solve Eq. 1 using a modified Levenberg-Marquardt method, using the errors for the radiance and irradiance as weights. The fit parameters are the slant columns $N_{s,O2O2}$ and $N_{s,O3}$, and c_R, and the coefficients for the polynomial $P(\lambda)$. In addition, also the diagnostics of the fit is obtained, including the residuals and error estimates for all fit parameters. The residuals are analyzed for possible outliers. Such outliers may be caused by high-energy particles hitting the detector or by varying dark current. Although al the information in the OMI Level 1B product is used to remove bad spectral pixels, some may remain. For outlier detection several methods have been used (e.g. Richter et al., 2011), which are mostly based on Gaussian statistics, i.e. by using the mean and standard deviation of the residual. Because particle hits will cause only increases in detected radiance and because the mean and standard deviation themselves are strongly affected by outliers, we selected the so-called box-plot method for outlier detection (http://www.itl.nist.gov/div898/handbook/prc/section1/prc16.htm). This method determines lower and upper values based on the 25th and 75th percentile of a distribution. If the lower quartile is $Q1$ and the upper quartile is $Q3$, then the difference $(Q3 - Q1)$ is called the interquartile range or IQ. We define outliers as those values smaller than $Q1 - 1.5\ IQ$ or larger than $Q3 + 1.5\ IQ$. After removal of the outliers, we redo the fitting of the spectrum to provide the final fit parameters. We have noted that the outlier removal is not stable; continuing iterating and each time applying the outlier removal procedure will often result in more and more removed spectral pixels. We therefore iterate only one time, thus removing the largest outliers.

Atmos. Meas. Tech. Discuss., doi:10.5194/amt-2016-48, 2016
Manuscript under review for journal Atmos. Meas. Tech.
Published: 6 April 2016

Atmospheric Measurement Techniques Discussions
Open Access

Conversion to Cloud and Scene Parameters

Radiative transfer modelling

For the conversion of the DOAS fit parameters into respectively cloud fraction and pressure, and scene albedo and scene pressure, we use radiative transfer modeling. The difference between the independent pixel approximation (IPA) (Zuidema and Evans, 1998) that determines the cloud fraction and pressure, and the Lambertian equivalent reflectance (LER) model that determines the scene albedo and pressure, is illustrated in Fig 1. It is noted that the clouds and the ground surface in the IPA model are treated as opaque Lambertian reflectors. Therefore, the name LER maybe somewhat confusing, but is used for consistency with the existing literature. For each ground pixel, both the IPA and LER method is applied. The IPA requires a-priori information on the surface reflectance and surface pressure. The clouds are represented as Lambertian reflectors with an albedo of 0.8. Different studies have found that this is an optimal choice for the purpose of cloud corrections in trace retrieval schemes (see (Stammes et al., 2008) and references therein). Using such a high albedo for the clouds will represent thin clouds covering the entire ground pixel as small cloud fraction. Thus, the cloud-free part will implicitly model the transmission of light through the cloud, which is otherwise absent in the Lambertian cloud model.

For very small cloud fractions the cloud pressure derived using the IPA will become undetermined. In case of surface albedo's close to 0.8, e.g. over snow and ice, the IPA retrieval for both cloud fraction and pressure will become undetermined. In such cases, the LER method may be a good fallback.

For both the IPA and LER model, we use the same set of forward model simulations of the reflectance between 460 and 490 nm, see Table 1. These simulations are performed for a mid-latitude summer standard atmosphere. The correction for different temperature profiles is discussed later on in this section. On the simulated reflectance the same DOAS fit is performed as for the measured OMI spectra (Eq. 1). For all the nodes listed in Table 1, we obtain the slant column O_2-O_2 as well as the continuum reflectance at 475 nm. The continuum is computed by evaluating the polynomial $P(\lambda)$ for this wavelength.

Look-up-table inversion

Although we now have the information needed to derive the cloud fraction/pressure and the scene albedo/pressure, we invert the tables to improve the computational speed. Instead of having the cloud fraction and cloud pressure as nodes of the tables, we want to have the slant column O_2-O_2 and continuum reflectance as nodes. This conversion process involves interpolation and extrapolation, for which we use linear radial basis functions (http://docs.scipy.org/doc/scipy-0.15.1/reference/generated/scipy.interpolate.Rbf.html).

Because the simulated spectra cover a very wide range of conditions, it is unlikely that the extrapolations in this inversion procedure have a large effect on the final result. The inversion is illustrated in Fig. 2. The final result of the inversion procedure are look-up tables (LUTs) for the cloud fraction, cloud pressure, scene albedo and scene pressure on the nodes listed in Table 2. In the retrieval algorithm linear interpolation is applied on all dimensions, except for the solar zenith angle, for which spline interpolation is applied. This is implemented because of the non-linear behavior at large solar zenith angles.

Temperature correction

As will be described in this section, the slant column amount of O_2-O_2 depends on the temperature profile, even if the cross section is not temperature dependent. This is due to the nature of the dimers, of which the absorption scales with the pressure-squared instead of being linear with pressure. Because this effect turns out to be significant, we have developed a temperature correction. This correction allows the use of the LUTs described above, which have been derived for a single pressure-temperature profile. By applying temperature correction, the O_2-O_2 slant columns are scaled to the values for the reference temperature profile that has been used to construct the LUTs.

To understand the temperature effect of the O_2-O_2 slant columns, we write the reflectance as:

$$R(\lambda) = R_0(\lambda) \exp\left(-\int_{z_0}^{TOA} m(z,\lambda)\, n_{O2}^2\, \sigma_{O2-O2}(\lambda)\, dz\right), \qquad (2)$$

where $R_0(\lambda)$ is the reflectance if absorption by O_2-O_2 is ignored; z_0 is the altitude of a Lambertian cloud or the Earth surface; *TOA* is he top of the atmosphere; $m(z,\lambda)$ is the altitude resolved air mass factor which is weakly wavelength dependent; $n_{O_2}(z)$ is the number density of oxygen and $\sigma_{O2-O2}(\lambda)$ is the absorption cross section of O_2-O_2.

In hydrostatic equilibrium, the integral over the altitude can be replaced by an integral over the pressure, using $dp/dz=-\rho(z)g$, where is the density of air. By expressing the density of air as $\rho(z)=M\,p\,/\,(Rg\,T(z))$, where M is the mean molecular mass of dry air and R_g is the gas constant, Eq. 2 becomes:

$$R(\lambda) = R_0(\lambda) \exp\left(\int_{p_0}^{p_{TOA}} \frac{R_g}{M\,g}\, T(p)\, m(p,\lambda)\, n_{O2}^2(p)\, \sigma_{O2-O2}(\lambda)\, \frac{dp}{p}\right). \qquad (3)$$

Finally, we can express the number density of air in as $n_{O_2} = 0.21\, p/(k_b\, T(p))$, where k_b is Boltzmann's constant and we assume a mixing ratio of oxygen of 21%. Substituting this in Eq. 3 gives:

$$R(\lambda) = R_0(\lambda) \exp\left((0.21)^2 \frac{R_g}{M\,g\,k_B^2} \sigma_{O2-O2}(\lambda) \int_{p_0}^{p_{TOA}} m(p,\lambda)\, \sigma_{O2-O2}(\lambda)\, \frac{p}{T(p)}\, dp\right), \qquad (4)$$

which shows that the reflectance and hence the slant column of O_2-O_2 changes when the temperature profile changes. It is noted that this is due to the density-squared nature of the absorption of O_2-O_2. For "normal" absorbers (no collision complex) the slant column is independent of the temperature profile, apart from temperature dependence of the absorption cross section.

In order to investigate the magnitude of the bias that is introduced if the temperature dependence is ignored simulations of the retrieval were performed. In the retrieval the mid-latitude summer profile is used while for the simulations either a mid-latitude winter profile or a sub-arctic winter profile is used. The bias was calculated for different true pressure levels of the cloud and for different cloud fractions. Fig 3 shows that the maximum bias in the retrieved cloud pressure ranges from less than 50 hPa at large cloud fractions to 200 hPa at very small cloud fractions. Such biases will have a significant impact on trace gas retrievals, which are commonly limited to scenes with small cloud fractions.

The OMCLDO2 retrieval is based on a LUT approach and generating LUTs for different temperature profiles in not feasible. Therefore we introduce a correction factor γ that translates the measured slant column into the slant column for the reference pressure-temperature profile. Using Eq 4., we can compute γ as:

$$\gamma = \frac{N_s^{ref}}{N_s^{meas}} = \frac{\int_{p_c}^{p_{TOA}} m(p,\lambda)\frac{p}{T_{ref}(p)}dp}{\int_{p_c}^{p_{TOA}} m(p,\lambda)\frac{p}{T(p)}dp} \tag{5}$$

where $T(p)$ is the actual temperature profile taken and $T_{ref}(p)$ is the temperature profile used in the creation of the look-up tables. In case of partial cloud cover and weak absorption we obtain

$$\gamma = \frac{N_s^{ref}}{N_s^{meas}} = \frac{(1-c_f)R_{clr}\int_{p_s}^{p_{TOA}} m_{clr}(p,\lambda)\frac{p}{T_{ref}(p)}dp + c_f R_{cld}\int_{p_c}^{p_{TOA}} m_{cld}(p,\lambda)\frac{p}{T_{ref}(p)}dp}{(1-c_f)R_{clr}\int_{p_s}^{p_{TOA}} m_{clr}(p,\lambda)\frac{p}{T(p)}dp + c_f R_{cld}\int_{p_c}^{p_{TOA}} m_{cld}(p,\lambda)\frac{p}{T(p)}dp} \tag{6}$$

where R is the reflectance at a representative wavelength in the fit window, p_s is the surface pressure and p_s the cloud pressure, and the subscripts *clr* and *cld* refer to the clear part and the cloudy part of the pixel, respectively.

To implement the temperature correction factor, new look-up-tables for the O_2-O_2 air mass factors $m(p,\lambda)$ and the corresponding reflectance for a wavelength in the middle of the fit window have been generated. In the retrieval algorithm, the temperature correction is applied in an iterative manner because the cloud fraction and pressure should be known to compute γ. As a default, we use three iterations to compute γ.

A-priori information

The OMCLDO2 version 2 uses the following *a-priori* information.

For the absorption cross-sections for O_2-O_2, ozone and optionally NO_2, as well as for the radiance Raman scattering, we use the spectra described in Van Geffen et al., (2015). For the surface reflectance, the OMI derived monthly mean database described in Kleipool et al., (2008) extended to 5 years of OMI data is used. For the temperature profiles needed for the temperature correction, we use a monthly mean climatology at four times per day (00, 06, 12 and 18 UTC), derived from the NCEP reanalysis data for the period 2005-2014. Actual temperatures maybe somewhat better than using a climatology. However for practical reasons related to the operational data processing facility, we have decided to use a temperature climatology. For detecting snow and sea-ice coverage, the Near-real-time Ice and Snow Extent (NISE) product (Nolin et al., 1998) is used.

Impact of algorithm updates

In this section we first compare the OMCLDO2 version 2 with the version 1.2.3 for one day of data. Next, the impacts of each of the improvements are discussed separately. The impact of the improvements are summarized in Table 2.

Figure 4 shows the OMCLDO2 retrieval results for 14 May 2005. This day has been selected arbitrarily from the OMI data record. Note that we also have analysed other days, which show consistent results. Figure 4a and b show the effective cloud fraction and the effective cloud pressure. Figures 4c and d show the difference between version 2 and version 1.2.3. For areas with low effective cloud fractions, the effective cloud fraction is approximately 0.01 higher in the version 2. Over the high latitudes in the northern hemisphere considerably large positive and negative differences occur. These occur over snow and ice, where the retrieval algorithm has problems to distinguish the clouds from the highly reflective surface. Under such conditions, the accuracy of the retrieved effective cloud fraction will be very low. Due to the assumed cloud albedo of 0.8, the cloud fraction will become undetermined when the surface albedo is also close to this value.

The differences in effective cloud pressure are shown in Fig 4d. Version 2 shows higher cloud pressure in the tropics and sub-tropics, and lower cloud pressures and mid and high latitudes. As discussed below, this zonally dependent effect is caused by the temperature correction introduced in version 2. Especially in the tropics, the differences in the cloud pressures are largest in regions with low cloud fractions. Overall the uncertainty in the cloud pressure retrievals is a strong function of the effective cloud fraction. This is illustrated in Figure 5, which shows the precision of the effective cloud pressure retrievals as a function of the effective cloud pressure. The precision is calculated by the propagation of the DOAS fit errors of the O_2-O_2 slant columns and of the continuum reflectance. For cloud fractions below 0.1 the average precision is larger than 20 hPa with a very large spread, whereas for cloud fractions above 0.9 the precision is less than 10 hPa with a much smaller spread. It is noted that other errors sources, for example in the *a priori* surface albedo will also have a much stronger impact at low effective cloud fractions.

Temperature correction

The correction for the temperature dependence is described above. Based on a temperature climatology, a correction factor is computed and applied to the O_2-O_2 slant columns. Figure 4g shows the temperature correction factor for the OMI observations on 14 May 2005. Because the temperature correction factor is computed relative to the midlatitude summer atmosphere, it is larger than 1 in the tropics and smaller at the higher latitudes. On top of this general behavior there is spatial structure related to cloud structures, especially when the clouds are at high altitudes and have significant optical thickness. The effect of clouds on the temperature correction factor is described in Eq. 6. For high and thick clouds the temperature correction is in most cases closer to 1, indicating that the largest differences between the climatological temperature and the mid-latitude summer atmosphere occurs at the lowest altitudes.

To test the impact of the temperature correction factor on the effective cloud fraction and pressure, we produced datasets with and without the temperature correction applied for two days of OMI data in different seasons (14 May 2005 and 15 November 2005). While the impact on the cloud fraction is negligible, the impact on the cloud pressure can be significant. Fig. 6 shows the difference between the retrievals without and with the correction applied, as a function of the effective cloud fraction. The impact of the correction on the cloud pressure increases towards smaller cloud fractions. Depending on whether the correction factor is smaller or larger than 1, the impact on the cloud pressure can be both positive or negative. For cloud fractions below 0.2, the impact of the temperature correction can be as large as -100 to 150 hPa, whereas for cloud fractions larger than 0.2 the impact is in the range -20 to 40 hPa. For the higher latitudes (γ>1) the clouds are at lower pressures (higher altitude) when the temperature correction is applied, whereas in the tropics and sub-tropics the effects is reversed.

Fig. 6 can be compared to Fig. 2, which is based on retrieval simulations. Although Fig. 6 shows the difference with and without the temperature corrections, and Fig. 2 shows the difference with the simulated truth, the behavior and magnitude of the bias is very similar. It is noted that for Fig. 2 only temperature profiles have been used which are colder in the troposphere than the reference mid-latitude summer atmosphere. Therefore, Fig 2 shows only positive biases, whereas in the tropics and sub-tropics Fig. 6 also shows negative values.

Look-up-tables

To test the impact of the LUTs that are used to derive the effective cloud fraction and effective cloud pressure, we produced a datasets using the version 2 algorithm with the new and the old LUTs. The cloud fraction with the new LUTs is about 0.01 larger than with the old version, except over snow and ice regions where the cloud fraction is in most cases significantly smaller. Because over snow and ice covered regions the cloud fraction is highly uncertain as the algorithm is not able to distinguish clouds from highly reflective surfaces, this impact is not unexpected.

The effect of the new LUTs on the effective cloud pressure is shown in Fig. 7c. This figure shows the difference in the cloud pressure (old minus new) as a function of the effective cloud pressure. The differences become significant at cloud fractions smaller than 0.25, where the difference shows an oscillating behavior. At a c_f of approximately 0.125 a minimum is reached and at smaller cloud fractions the mean difference reverses sign and increases towards lower c_f. To investigate the nature of this behavior, Fig. 7a and 7b show the distribution of the retrieved cloud pressures as a function of cloud fraction for the old and new LUT datasets. From these figures it is clear that the origin of the oscillating behavior of the difference is in the retrievals with the old LUTs. Fig 7a shows that with the old LUTs the cloud pressure increasing strongly towards lower cloud fractions, for which we have no physical explanation. The results with the new LUTs (Fig. 7b) do not show this. We attribute the large improvements with the new LUTs to the larger number of radiative transfer calculations on which it is based, as well as the improved interpolation scheme that was used to produce it.

Figs. 7a and 7b also show that the effective cloud pressure for the largest c_f bin is significantly larger. A further inspection showed that this is caused retrievals over snow and ice covered regions, for which the cloud pressure retrievals are highly uncertain. For such cases the scene albedo and pressure provided by the version 2 algorithm can be used.

Atmos. Meas. Tech. Discuss., doi:10.5194/amt-2016-48, 2016
Manuscript under review for journal Atmos. Meas. Tech.
Published: 6 April 2016

Outlier removal

The outlier removal procedure that was introduced in the version 2 of the algorithm removes spectral pixels from the DOAS fit after evaluation of the fitting residuals. Outliers can have different behavior: they can be transient, e.g. occurring only for spectral pixels for a few pixels, or they can occur systematically for certain spectral pixels. When outliers are detected they are removed from the data, which will decrease the number of wavelengths used in the DOAS fit. Fig. 4h shows the number of wavelengths used in the fit for 14 May 2005. The most prominent feature are the reduced values over the South America caused by the South Atlantic Anomaly (SAA). In this region the number of high energetic particles hitting the OMI detectors is significantly increased (Dobber et al., 2006), resulting in spikes in the data. It is noted that also the Level 0-1B processor flags transient pixels, so Fig. 4h is the result of the Level 1B flags in combination with the outlier removal procedure. In addition to the SAA, figure 4h also shows stripes in the along-track direction, as well as features related to geophysical conditions (for example higher values of Australia and the India).

The impact of the outlier removal procedure was tested by running the algorithm with and without the procedure switched on for 14 May 2005. The differences in the retrieved effective cloud fraction are negligible, whereas the impact on the effective cloud pressure depends on the cloud fraction. The mean difference is not significant, but the standard deviation of the difference varies for 16 hPa for $c_f < 0.2$ to 3 hPa for $c_f < 0.8$.

We also inspected the root-mean-square error (RMSE) of the DOAS fit as a fit quality indicator. Although the difference in RMSE with and without the outlier removal did not differ significantly from zero, the distribution is skewed towards larger RMSE values when the outlier removal is switched off. This indicates that the outlier removal procedure improves the fit for cases with a high RMSE.

Digital Elevation Model

The version 2 of the algorithm uses a DEM with a resolution of approximately 20 km, which is closer to the spatial resolution of OMI compared to the 3 km resolution DEM used in previous versions. The 20 km resolution DEM is constructed from the Global Multi-resolution Terrain Elevation Data 2010 (Danielson and Gesch, 2011).

The impact of the new DEM will be largest in mountainous terrain. Fig. 8 illustrates the effect on the retrieved effective cloud pressures over Europe for 14 May 2005. This is the same day as shown in Fig. 4. Fig. 8a shows that significant impacts of the new DEM are restricted to the main mountain ranges. The difference between using the old and new DEM can be both positive and negative. The impact increases towards the lower cloud fractions, when more signal comes from the surface and an accurate knowledge of the surface altitude becomes more important. Fig 8b shows that for most pixels the impact is smaller than ±50 hPa.

Cross sections

In the new version of the algorithm, absorption cross-sections and the Raman radiance spectrum have been updated. The impact of this change was tested by running the algorithm with the old and the new cross sections. The impact on the cloud fraction was negligible. Using the new cross sections increased the effective cloud fractions by 23±23 hPa. The difference in the root-mean-square error of the DOAS was not significant. The new cross-sections didn't significantly reduce the residuals of the DOAS fit.

Scene albedo and scene pressure

As described in the algorithm section, for each ground pixel the scene albedo and scene pressure is derived. The most important application of these parameters is over bright surfaces such as snow and ice, where the surface albedo becomes close to the assumed cloud albedo of 0.8 and no meaningful cloud fraction and pressure can be derived. Fig. 9 shows a comparison of the retrieved scene pressure with the surface pressure derived from the DEM, assuming a sea level pressure of 1013 hPa. The figure shows a very good agreement between the retrieved scene pressure and the DEM over Greenland. This figure presents the comparison for the OMI cross track pixel 20, but other cross pixels show similar results. It demonstrates the capabilities of the scene pressure for bright surfaces. Also, it is an indirect validation of the retrieved O_2-O_2 slant columns. A correction of the O_2-O_2 slant columns, as is sometimes used in ground based DOAS measurements (for a discussion see (Spinei et al., 2015)), is clearly not necessary for the OMI retrievals.

Over dark surface, such as oceans, the scene pressure is less well understood. For some areas over the ocean the retrieved scene pressure is significantly larger than the sea level pressure. Therefore, we recommend using the scene albedo and scene pressure only for ground pixels which are covered with snow and/or ice.

Comparison with ground-based radar

The changes made in the version 2 of the OMCLDO2 algorithm have a stronger impact on the cloud pressure retrieval then on the cloud fraction retrieval. Therefore, we focus in this section on comparisons of the cloud pressure retrievals with correlative data. Because of the use of the IPA cloud model (Fig. 1), it is not straightforward to compare the retrieved cloud pressure to profile information on cloud parameters. As discussed below, we compare the OMI retrievals with ground based radar data, for which the sensitivity to cloud droplet size is very different; the OMI retrievals are sensitive to the optical extinction with scales with droplet size to the power 2, whereas the radar reflectivity scales with droplet size to the power 6. Thus, using these radar data it is not possible to compare the same quantity, which is required in a validation study. Rather than a validation study, we focus on explaining the differences between the OMI retrievals and the radar data, given their different sensitivities. This comparison uses a similar approach as was used for comparing SCIAMACHY cloud products with radar data (Wang and Stammes, 2014).

We present comparisons for three sites: Cabuw, The Netherlands, Lindenberg, Germany and the ARM Southern Great Plains, U.S.A., for the period January to June 2006. These datasets were selected because of the continuous data availability for these sites in the Cloudnet datatabase.

Atmos. Meas. Tech. Discuss., doi:10.5194/amt-2016-48, 2016
Manuscript under review for journal Atmos. Meas. Tech.
Published: 6 April 2016

Atmospheric Measurement Techniques Discussions

Cloudnet data

The Cloudnet dataset is the Level 2 classification product (Illingworth et al., 2007), which is available approximately every 30 seconds. This product classifies each vertical layer as one of 11 classes, which distinguish ice and water clouds, precipitation, aerosols, insects, clear sky and combinations thereof. We attribute a value of 1 to layers that are classified as cloudy (classes 1-7) and 0 to layers identified as non-cloudy. For profiles containing at least one cloudy layer, we compute the cloud mid-height as the average of the altitude of the cloudy layers. Next we average all the profiles in the time window of +/- 30 minutes of an OMI overpass. We also compute the average and standard deviation of the cloud mid-height over this time window and determine for the average cloud profile if it is single-layer or multi-layer.

It is noted that this procedure for computing the cloud mid-height doesn't take the optical thickness of the layers into account; a optically thick cloud and optically thin cloud are weighted the same in the cloud mid-height. Weighting with the optical thickness - or even better, with the sensitivity of the O_2-O_2 cloud algorithm- would make a comparison much more direct. Unfortunately, information on the full optical thickness profile is not available from the Cloudnet data. Alternatively, we could use the radar reflectivity as weighting parameter. However the radar reflectivity is very sensitive to cloud particle size, which is also not a good representation for the cloud extinction in the visible. We therefore decided to use the simple weighting described above. This weighting gives the same weight to optically thin cloud layer as to optically thick layers, whereas the O_2-O_2 is cloud pressure retrieval is much more sensitive to the thick layers.

Further filtering of the Cloudnet data was done using the following criteria:

- The standard deviation of the cloud-mid height should not exceed 1.5 km, to avoid cases with large temporal variability during the OMI overpass;
- At least one layer in the profile should be cloudy during at least 50% of the time averaging window.

OMI collocated data

For the OMI cloud data we average all the ground pixels of which the center is within 30 km distance of the ground station. For these pixels we determine the mean and standard deviation for the cloud fraction and pressure. We convert the cloud pressure to altitude using a scaling height of 8 km. We filter the OMI data using the following criteria:

- The effective cloud fraction should exceed 0.2, because the cloud pressure for low cloud fraction has a large uncertainty;
- The standard deviation of effective cloud pressures should not exceed 1.5 km, to exclude cases with large horizontal variability.

Results

Figure 10 shows a comparison between the Cloudnet data and the OMI effective cloud pressure for the collocations over Cabauw for the period January to June 2006. The cases presented in this figure are ordered by increasing mid-height of ground-based data. The following regimes can be distinguished in this data set:

Atmos. Meas. Tech. Discuss., doi:10.5194/amt-2016-48, 2016
Manuscript under review for journal Atmos. Meas. Tech.
Published: 6 April 2016

1. Case 1-50: These are low level clouds with limited vertical extent. The OMI effective cloud height and the ground stations mid-height are in good agreement.
2. Case 51-129: According to the Cloudnet the majority of these cases consist of vertically extended, and often multi-layered cases. For these cases the OMI effective cloud height is generally lower than the ground station mid-height.
3. Case 130-135: Theses cases have high clouds with limited vertical extent. The OMI effective cloud height compares well, except for the outlier for cases 131. However, the number of collocations in this regime is small.

It is noted that the boundaries of these three regimes are not hard.

Figure 10 shows that for single layer clouds with a limited vertical extent, the O_2-O_2 effective cloud height and the Cloudnet derived mid-height are in agreement. This shows that the OMI derived product is capable of retrieving cloud height ranging from low clouds to high clouds. For vertically extended clouds, the OMI derived cloud heights are generally lower than the radar-lidar derived heights. A plausible explanation for this difference is that in these cases there are thin high clouds overlaying thicker low-level water clouds. Whereas the radar-lidar mid-heights have equal sensitivity, the O2-O2 cloud height will be more sensitive to the optically thick layers.

When we include not only Cabauw, but also Lindenberg and the ARM-SGP site, we get a similar picture. Figure 11 shows a comparison for all these sites for the period January-June 2006, where the single and multi-layer cloud cases are distinguished. Good correlation is observed for the cloud range of 0-2.5 km, where the single-cloud layers dominate. In the region between 2.5 and approximately 8 km the multi-layer clouds dominate and the O_2-O_2 cloud-height is lower than the radar-lidar cloud mid-height. Above 8 km we find both good comparison but also very large differences, although the number of points is very limited. As we are interested in the average comparisons, we did not investigate individual cases where big differences occurred.

Conclusions

We present a new version of the OMI OMCLDO2 Level 2 cloud product. This product is an important input for several of the operational OMI Level 1-2 algorithms. The new version contains six major improvements

1. The correction for the temperature sensitivity of the DOAS fit;
2. Improved look-up-tables for computing the effective cloud fraction and effective cloud pressure;
3. Retrieval of the scene pressure and scene albedo for every ground pixel, using the Lambertian Equivalent Reflector model;
4. Outlier removal procedure in the DOAS fit.
5. Updated of the reference cross sections;
6. Introduction of a DEM with a similar spatial resolution as the OMI ground pixels.

We show that the impact of these changes on the retrieved effective cloud fraction is for most ground pixels less than 0.01. The impact on the effective cloud pressure is larger: especially for cloud fractions less than approximately 0.3 the differences compared to the previous operational version can be as large

Atmos. Meas. Tech. Discuss., doi:10.5194/amt-2016-48, 2016
Manuscript under review for journal Atmos. Meas. Tech.
Published: 6 April 2016

as 200 hPa. These differences are mainly caused by the temperature correction and the introduction of the new look-up tables. Due to the temperature the differences have a latitudinal and seasonal dependent behavior, where the updated algorithm gives higher cloud pressures at higher latitudes and lower pressures in the tropics and sub-tropics. Also it was found that the new look-up-tables gives better results at low cloud fractions.

Cloud pressure retrievals have been compared to ground based radar-lidar observations in Cabauw, Lindenberg and the ARM-SGP site. It was found that for low clouds, up to approximately 2.5 km, the satellite retrievals and ground-based results compare favorably. For clouds in the range between 2.5 and approximately 8 km the ground-based observations indicate many multi-layer and vertically extensive clouds. For these clouds the satellite retrieved cloud heights are generally lower, probably because the algorithm is more sensitive to the optically thick low-level clouds. For high clouds (>8 km) mixed results are found. The differences with the lidar-radar can be explained by the different sensitivity of the lidar-radar observations versus the satellite observations.

We conclude that the new version of the OMCLDO2 product is a significant improvement of the previous versions, especially for the cloud pressure at cloud fractions smaller than approximately 0.3. This is very important for cloud corrections in retrievals of gases like nitrogen dioxide, sulphur dioxide and formaldehyde, which are very sensitive to the cloud pressure.

After the reprocessing of the entire OMI data record, the stability of the product should be investigated, and the scene pressure and scene albedo should be validated.

Acknowledgements

This work was funded by the Netherlands Space Office under the science OMI contract.

We acknowledge the EU Cloudnet and the ACTRIS projects for providing the cloud classification dataset, using Radar-Lidar cloud classification products for the Cabauw, Lindenberg and the ATM-SGP sites.

References

Acarreta, J. R., De Haan, J. F. and Stammes, P.: Cloud pressure retrieval using the O_2–O_2 absorption band at 477 nm, jgr, 109(D5), doi:10.1029/2003JD003915, 2004.

Boersma, K. F., Eskes, H. J., Dirksen, R. J., van der A, R. J., Veefkind, J. P., Stammes, P., Huijnen, V., Kleipool, Q. L., Sneep, M., Claas, J., Leitão, J., et al.: An improved tropospheric NO2 column retrieval algorithm for the Ozone Monitoring Instrument, Atmospheric Meas. Tech., 4(9), 1905–1928, doi:10.5194/amt-4-1905-2011, 2011.

Bogumil, K., Orphal, J. and Burrows, J. P.: Temperature dependent absorption cross sections of O3 , NO2 , and other atmospheric trace gases measured with the SCIAMACHY spectrometer, in Looking down to Earth in the New Millennium, vol. SP-461, Gothenburg., 2000.

Danielson, J. J. and Gesch, D. B.: Global Multi-resolution Terrain Elevation Data 2010 (GMTED2010), U.S. Geological Survey. [online] Available from: http://topotools.cr.usgs.gov/gmted_viewer/, 2011.

Atmos. Meas. Tech. Discuss., doi:10.5194/amt-2016-48, 2016
Manuscript under review for journal Atmos. Meas. Tech.
Published: 6 April 2016

Dobber, M. R., Dirksen, R. J., Levelt, P. F., Van Den Oord, G. H. J., Voors, R. H. ., Kleipool, Q., Jaross, G., Kowalewski, M., Hilsenrath, E., Leppelmeier, G. W. and others: Ozone monitoring instrument calibration, Geosci. Remote Sens. IEEE Trans. On, 44(5), 1209–1238, 2006.

van Geffen, J. H. G. M., Boersma, K. F., Van Roozendael, M., Hendrick, F., Mahieu, E., De Smedt, I., Sneep, M. and Veefkind, J. P.: Improved spectral fitting of nitrogen dioxide from OMI in the 405-465 nm window, Atmospheric Meas. Tech., 8(4), 1685–1699, doi:10.5194/amt-8-1685-2015, 2015.

Geffen, J. van, Eskes, H., Boersma, K. F., Pedergnana, M., Sneep, M. and Apituley, A.: Sentinel-5 precursor/TROPOMI Level 2 Product User Manual Nitrogen Dioxide, KNMI., 2014.

Illingworth, A. J., Hogan, R. J., O'Connor, E. J., Bouniol, D., Delanoë, J., Pelon, J., Protat, A., Brooks, M. E., Gaussiat, N., Wilson, D. R., Donovan, D. P., et al.: Cloudnet, Bull. Am. Meteorol. Soc., 88(6), 883–898, doi:10.1175/BAMS-88-6-883, 2007.

Joiner, J., Vasilkov, A. P., Gupta, P., Bhartia, P. K., Veefkind, P., Sneep, M., de Haan, J., Polonsky, I. and Spurr, R.: Fast simulators for satellite cloud optical centroid pressure retrievals; evaluation of OMI cloud retrievals, Atmospheric Meas. Tech., 5(3), 529–545, doi:10.5194/amt-5-529-2012, 2012.

Joiner, J. and Vassilkov, A. P.: First Results From the OMI Rotational Raman Scattering Cloud Pressure Algorithm, ieeegrs, 44(5), 1272–1282, doi:10.1109/TGRS.2005.861385, 2006.

Kleipool, Q. L., Dobber, M. R., de Haan, J. F. and Levelt, P. F.: Earth surface reflectance climatology from 3 years of OMI data, jgr, 113, D18308, doi:10.1029/2008JD010290, 2008.

Levelt, P. F., van den Oord, G. H. ., Dobber, M. R., Malkki, A., Visser, H., de Vries, J., Stammes, P., Lundell, J. O. . and Saari, H.: The ozone monitoring instrument, IEEE Trans Geosc Rem Sens, 44(5), 1093–1101, 2006.

Nolin, A., Armstrong, R. and Maslanik, J.: Near-Real-Time SSM/I-SSMIS EASE-Grid Daily Global Ice Concentration and Snow Extent. Version 4., NASA National Snow and Ice Data Center Distributed Active Archive Center, Boulder, Colorado, USA. [online] Available from: http://dx.doi.org/10.5067/VF7QO90IHZ99, 1998.

Richter, A., Begoin, M., Hilboll, A. and Burrows, J. P.: An improved NO2 retrieval for the GOME-2 satellite instrument, Atmospheric Meas. Tech., 4(6), 1147–1159, doi:10.5194/amt-4-1147-2011, 2011.

Sneep, M., de Haan, J. F., Stammes, P., Wang, P., Vanbauce, C., Joiner, J., Vasilkov, A. P. and Levelt, P. F.: Three-way comparison between OMI and PARASOL cloud pressure products, J. Geophys. Res. Atmospheres, 113(D15), n/a–n/a, doi:10.1029/2007JD008694, 2008.

Spinei, E., Cede, A., Herman, J., Mount, G. H., Eloranta, E., Morley, B., Baidar, S., Dix, B., Ortega, I., Koenig, T. and Volkamer, R.: Ground-based direct-sun DOAS and airborne MAX-DOAS measurements of the collision-induced oxygen complex, O_2O_2, absorption with significant pressure and temperature differences, Atmospheric Meas. Tech., 8(2), 793–809, doi:10.5194/amt-8-793-2015, 2015.

Stammes, P., Sneep, M., de Haan, J. F., Veefkind, J. P., Wang, P. and Levelt, P. F.: Effective cloud fractions from the Ozone Monitoring Instrument: Theoretical framework and validation, jgr, 113, D16S38, doi:10.1029/2007JD008820, 2008.

Thalman, R. and Volkamer, R.: Temperature dependent absorption cross-sections of O2-O2 collision pairs between 340 and 630 nm and at atmospherically relevant pressure, Phys Chem Chem Phys, 15(37), 15371–15381, doi:10.1039/C3CP50968K, 2013.

Atmos. Meas. Tech. Discuss., doi:10.5194/amt-2016-48, 2016
Manuscript under review for journal Atmos. Meas. Tech.
Published: 6 April 2016

Voors, R., Dobber, M., Dirksen, R. and Levelt, P.: Method of calibration to correct for cloud-induced wavelength shifts in the Aura satellite's Ozone Monitoring Instrument, Appl Opt, 45(15), 3652–3658, doi:10.1364/AO.45.003652, 2006.

Wang, P. and Stammes, P.: Evaluation of SCIAMACHY Oxygen A band cloud heights using Cloudnet measurements, Atmospheric Meas. Tech., 7(5), 1331–1350, doi:10.5194/amt-7-1331-2014, 2014.

Wang, P., Stammes, P., van der A, R., Pinardi, G. and van Roozendael, M.: FRESCO+: an improved O2 A-band cloud retrieval algorithm for tropospheric trace gas retrievals, Atmospheric Chem. Phys., 8(21), 6565–6576, doi:10.5194/acp-8-6565-2008, 2008.

Zuidema, P. and Evans, K. F.: On the validity of the independent pixel approximation for boundary layer clouds observed during ASTEX, J. Geophys. Res. Atmospheres, 103(D6), 6059–6074, doi:10.1029/98JD00080, 1998.

Tables

Table 1: Nodes for the radiative transfer calculations. Note that cloud fractions smaller than 0 and larger than 1 are included to enlarge the parameters space.

Parameter	Nodes
solar zenith angle [°]	0.0, 9.3, 21.2, 32.9, 44.2, 54.9, 64.8, 73.5, 80.8, 86.1
viewing zenith angle [°]	0.0, 9.3, 21.2, 32.9, 44.2, 54.9, 64.8, 73.5
relative azimuth angle [°]	0, 30, 60, 90, 120, 150, 180
surface albedo	0.0, 0.01, 0.025, 0.05, 0.075, 0.1, 0.15, 0.2, 0.25, 0.325, 0.4, 0.5, 0.6, 0.7, 0.8, 0.9, 1.0
surface/cloud pressure [hPa]	1013, 963, 913, 863, 813, 763, 713, 663, 613, 563, 513, 463, 413, 363, 313, 263, 213, 163, 113, 63
cloud fraction	-0.1, -0.05, 0., 0.01, 0.02, 0.04, 0.06, 0.08, 0.1, 0.125, 0.15, 0.175, 0.2, 0.25, 0.3, 0.35, 0.4, 0.45, 0.5, 0.55, 0.6, 0.65, 0.7, 0.75, 0.8, 0.85, 0.95, 1.0, 1.1, 1.2

Table 2: Nodes for the continuum reflectance and the slant Column O2-O2, for the cloud fraction/pressure and scene albedo/scene pressure look-up-tables. The solar zenith angle, viewing zenith angle, relative azimuth angle, surface albedo and surface/cloud pressure nodes are the same as given in Table 1.

Parameter	Nodes
Continuum reflectance R_c at 477 nm	0.00, 0.05, 0.10, 0.15, 0.20, 0.25, 0.30, 0.35, 0.40, 0.45, 0.50, 0.55, 0.60, 0.65, 0.70, 0.75, 0.80, 0.85, 0.90, 0.95, 1.00, 1.05, 1.10, 1.15, 1.20, 1.25, 1.50, 1.75, 2.00
Slant Column O_2-O_2 [10^{44} molec^2 cm^{-5}]	0.00, 0.05, 0.10, 0.15, 0.20, 0.25, 0.30, 0.35, 0.40, 0.45, 0.50, 0.55, 0.60, 0.65, 0.70, 0.75, 0.80, 0.85, 0.90, 0.95, 1.00, 1.10, 1.20

Atmos. Meas. Tech. Discuss., doi:10.5194/amt-2016-48, 2016
Manuscript under review for journal Atmos. Meas. Tech.
Published: 6 April 2016

Table 3. Impact of the improvements of the effective cloud fraction and effective cloud pressure retrievals.

Improvement	**Impact on p_{cld}**	**Impact on c_f**
Temperature correction	Decreasing at higher latitudes Increasing in the tropics and sub-tropics Δp_{cld} : -100 to 150 hPa for $c_f < 0.2$ Δp_{cld} : -20 to 40 hPa for $c_f > 0.2$	negligible
New look-up-tables	Impact is non-significant for $c_f > 0.3$ Δp_{cld} : -60 to 220 hPa for $c_f < 0.3$	Δc_f : -0.01 except for high surface reflectivity for which $\Delta c_f > 0.05$
Outlier removal	No systematic impact	negligible
DEM	Impact restricted to mountainous terrain. Δp_{cld} for most pixels smaller than +/- 25 hPa	negligible
Cross-sections	Δp_{cld} : 23 +/- 23 hPa	negligible

Atmos. Meas. Tech. Discuss., doi:10.5194/amt-2016-48, 2016
Manuscript under review for journal Atmos. Meas. Tech.
Published: 6 April 2016

Figures

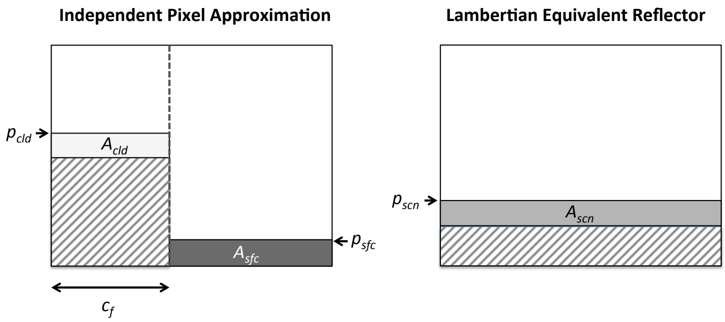

Figure 1: The Independent Pixel Approximation versus the Lambertian Equivalent Reflector model. In the IPA a ground pixel is modeled as the weighted sum of a cloudy part, (a Lambertian surface with an albedo of A_{cld} at a pressure level p_{sfc}) and a clear part (a Lambertian surface with an albedo of A_{sfc} at a pressure level p_{sfc}). The effective cloud fraction c_f is used for the weighting of the cloudy and clear contributions. The IPA method uses *a priori* information on A_{sfc}, A_{cld} and p_{sfc}. In the LER model the ground pixel is modeled as a Lambertian surface with a albedo A_{scn} at a pressure level p_{scn}. The LER method doesn't rely on *a priori* information. Note that the hatched areas below the opaque Lambertian indicate that these regions do not contribute in the radiative transfer calculations.

Atmos. Meas. Tech. Discuss., doi:10.5194/amt-2016-48, 2016
Manuscript under review for journal Atmos. Meas. Tech.
Published: 6 April 2016

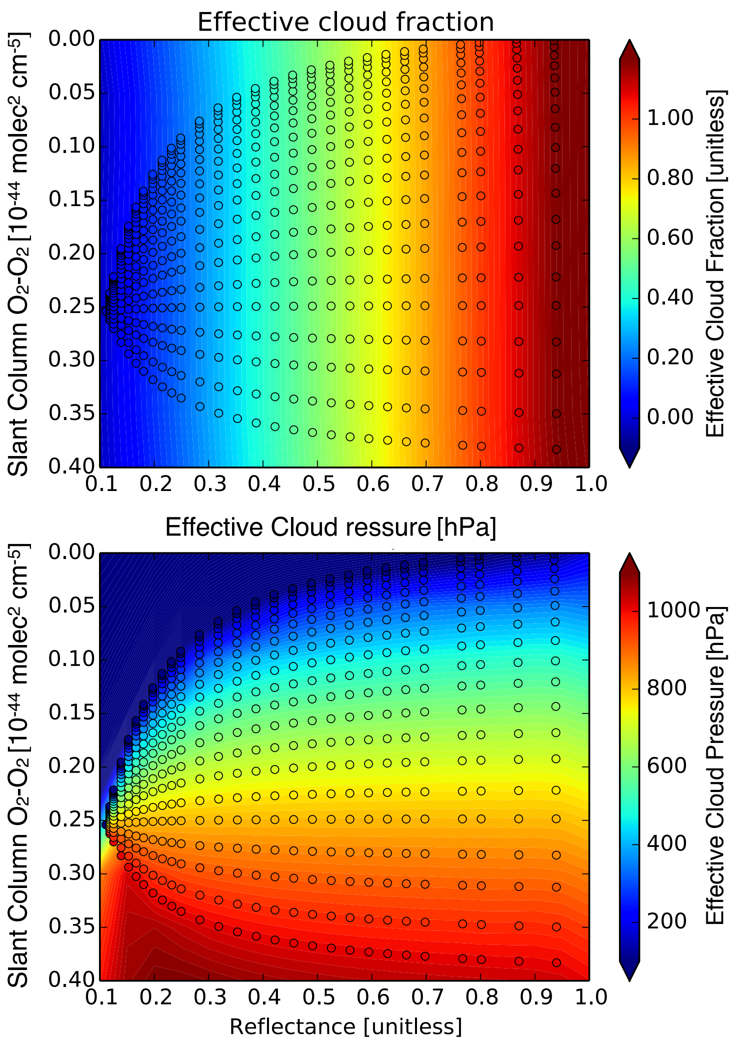

Figure 2: Example of a slice of the effective cloud fraction LUT (top panel) and effective cloud pressure LUT (bottom panel), showing the LUT value as a function of the continuum reflectance ρ_c and the slant column O_2-O_2 $N_{s,O2O2}$. The background colors show the values in the LUT derived from interpolation and extrapolation of the DOAS fit results, which are shown as the color-filled symbols. The other LUT nodes are fixed to the following values: solar zenith angle 44.2°; viewing zenith angle 21.2°; relative azimuth angle 0.0°; surface albedo 0.05; surface altitude 0 m.

Atmos. Meas. Tech. Discuss., doi:10.5194/amt-2016-48, 2016
Manuscript under review for journal Atmos. Meas. Tech.
Published: 6 April 2016

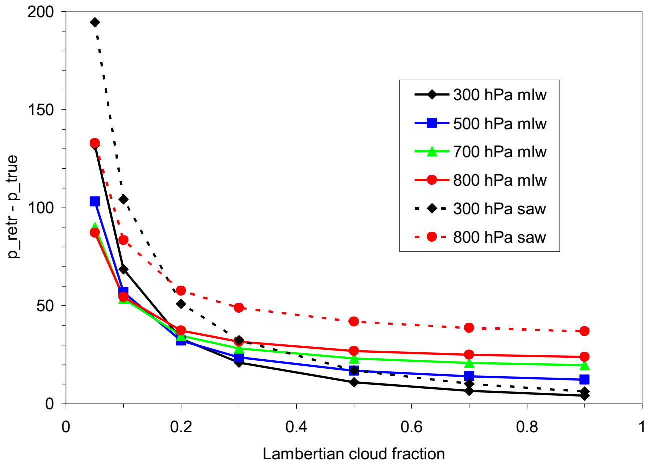

Figure 3: Bias in the retrieved pressure ($p_{retr} - p_{true}$) in hPa when in the retrieval a mid-latitude summer temperature profile is used whereas in the simulation a mid-latitude winter profile (mlw) or a sub-arctic winter profile (saw) is used. The results are plotted as a function of the cloud fraction and for different pressure levels of the cloud used in the simulation. The surface albedo is fixed at 0.05, the cloud albedo is 0.80, the solar zenith angle is 60 degrees and the viewing direction is nadir.

Atmos. Meas. Tech. Discuss., doi:10.5194/amt-2016-48, 2016
Manuscript under review for journal Atmos. Meas. Tech.
Published: 6 April 2016

Atmospheric Measurement Techniques
Open Access
Discussions

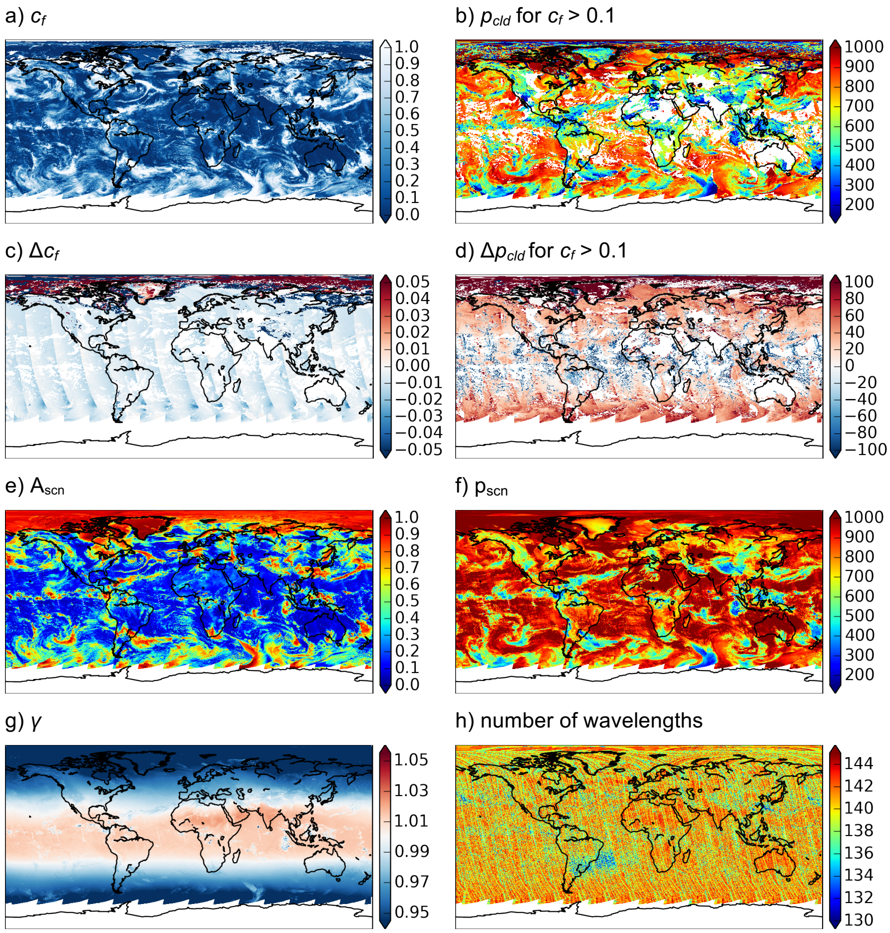

Figure 4: Results from the OMCLDO2 version 2 algorithm for 14 May 2005. a) effective cloud fraction, b) effective cloud pressure, c) difference of the effective cloud fraction (version 1.2.3 minus version 2), d) difference of the effective cloud pressure (version 1.2.3 minus version 2), e) scene albedo, f) scene pressure, g) SCD temperature correction factor γ, and h) number of wavelengths used in the DOAS fit.

Atmos. Meas. Tech. Discuss., doi:10.5194/amt-2016-48, 2016
Manuscript under review for journal Atmos. Meas. Tech.
Published: 6 April 2016

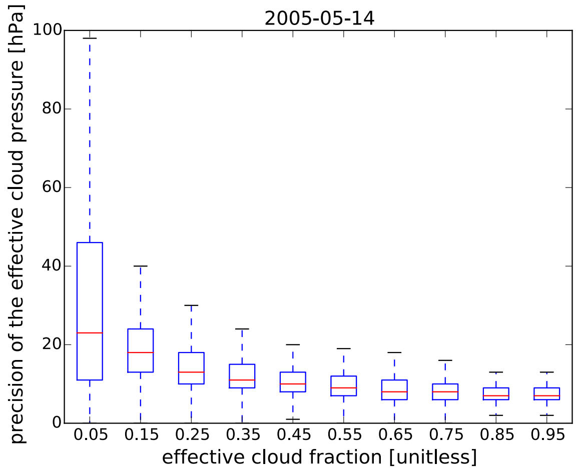

Figure 5: Box-whisker plot of the precision of the effective cloud pressure as a function of the effective cloud fraction for 14 May 2005.

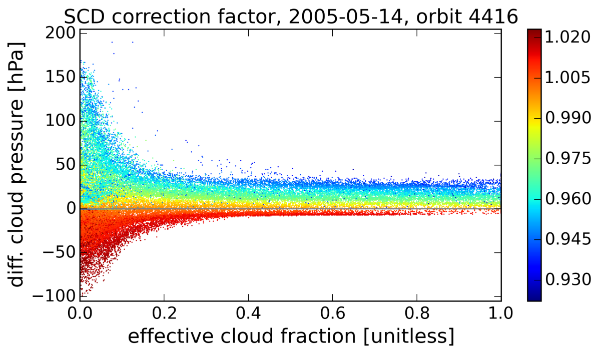

Figure 6: Difference in the effective cloud pressure due to the temperature correction (without correction minus with correction) plotted as function of the effective cloud fraction. The colors of the symbols indicate the SCD correction factor.

Atmos. Meas. Tech. Discuss., doi:10.5194/amt-2016-48, 2016
Manuscript under review for journal Atmos. Meas. Tech.
Published: 6 April 2016

Atmospheric Measurement Techniques Discussions
Open Access

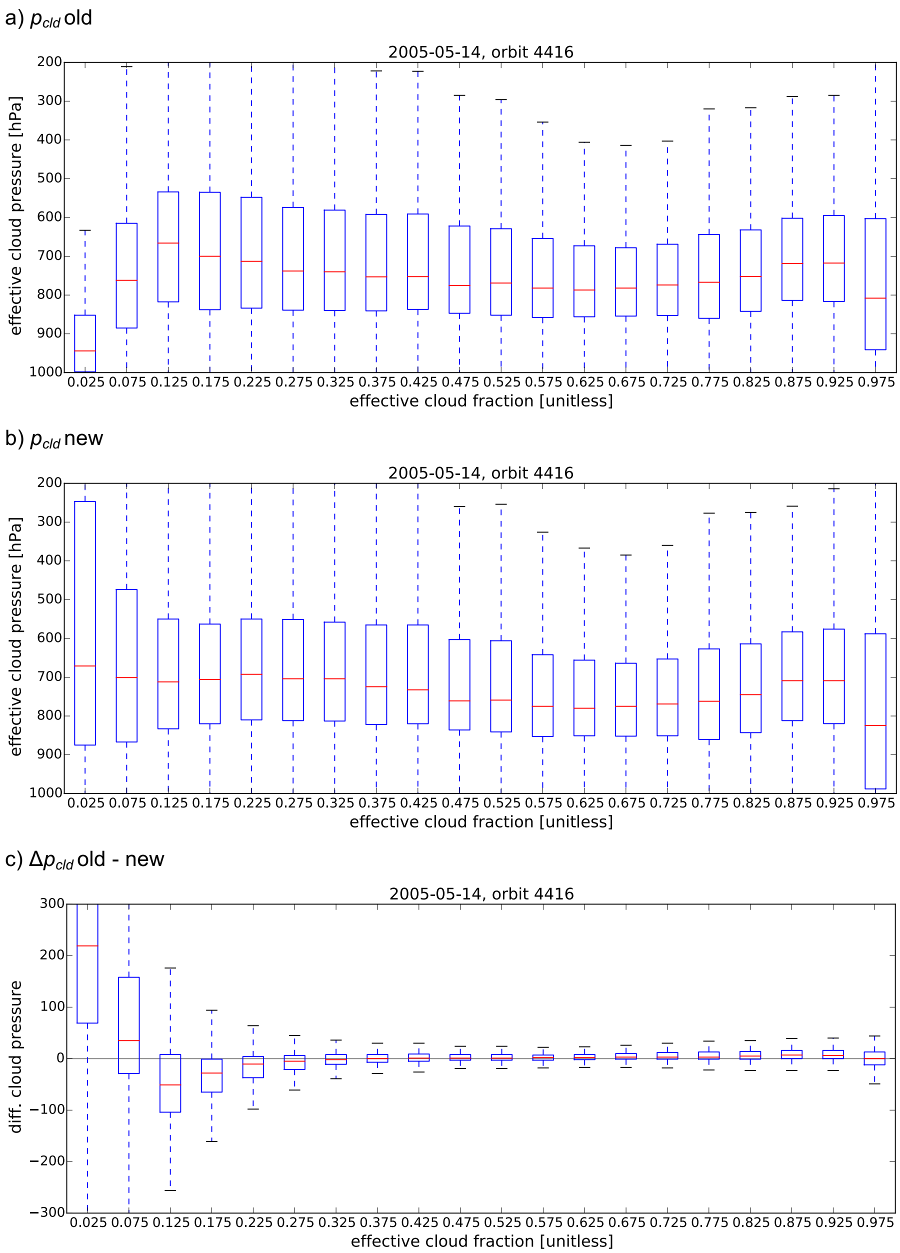

Figure 7: Box-whisker plots of the effective cloud pressure as a function of the effective cloud fraction. The top plot is for the old LUTs, the middle for the new LUTs and the bottom plot for the difference of old minus new.

Atmos. Meas. Tech. Discuss., doi:10.5194/amt-2016-48, 2016
Manuscript under review for journal Atmos. Meas. Tech.
Published: 6 April 2016

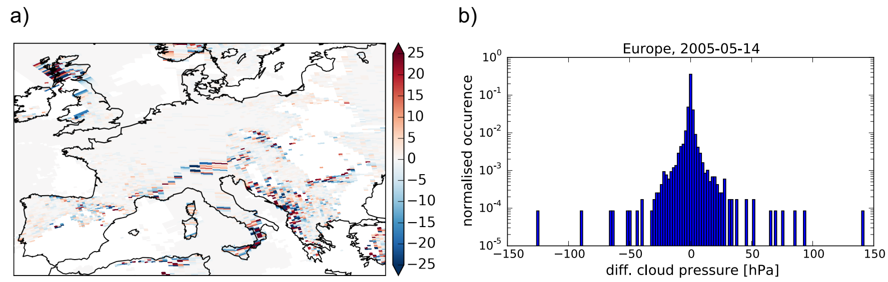

Figure 8: Difference in the effective cloud pressure (old DEM minus new DEM) for effective cloud fractions exceeding 0.1 over Europe for 14 May 2005. Left panel: map of the differences over Europe, right panel: histogram of the differences over Europe on a logarithmic scale.

Atmos. Meas. Tech. Discuss., doi:10.5194/amt-2016-48, 2016
Manuscript under review for journal Atmos. Meas. Tech.
Published: 6 April 2016

Atmospheric Measurement Techniques
Discussions

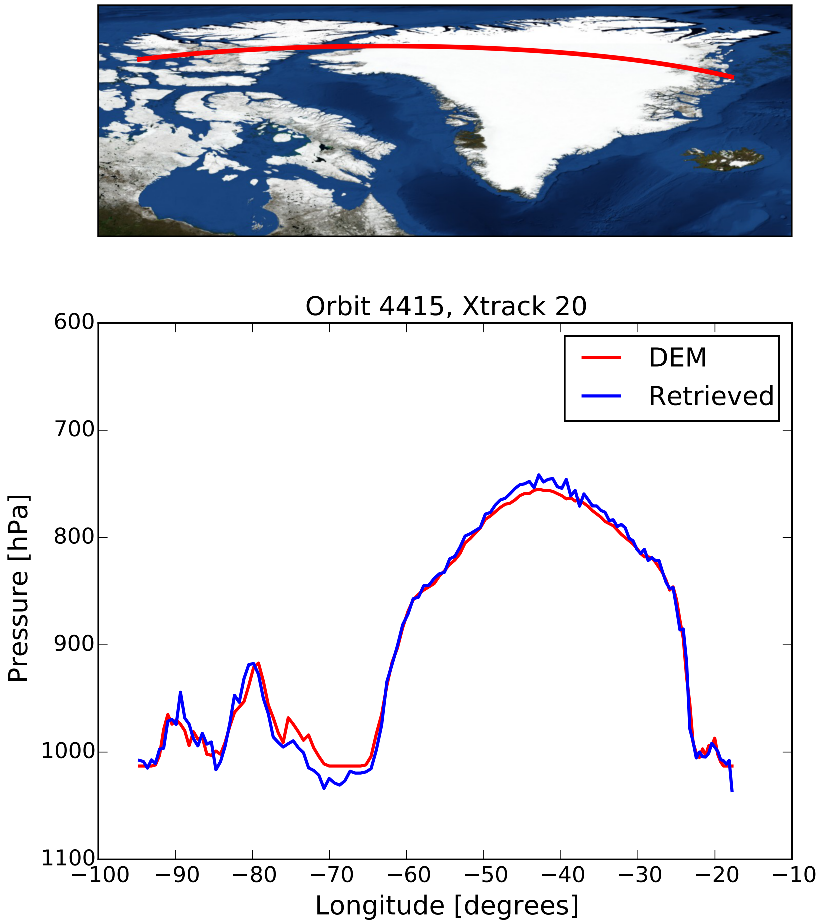

Fig 9: Top panel: map of the position of the ground pixels centers. Bottom panel: comparison of the retrieved scene pressure and the surface pressure derived from the DEM, plotted as a function of the longitude.

Atmos. Meas. Tech. Discuss., doi:10.5194/amt-2016-48, 2016
Manuscript under review for journal Atmos. Meas. Tech.
Published: 6 April 2016

Atmospheric Measurement Techniques
Open Access
Discussions

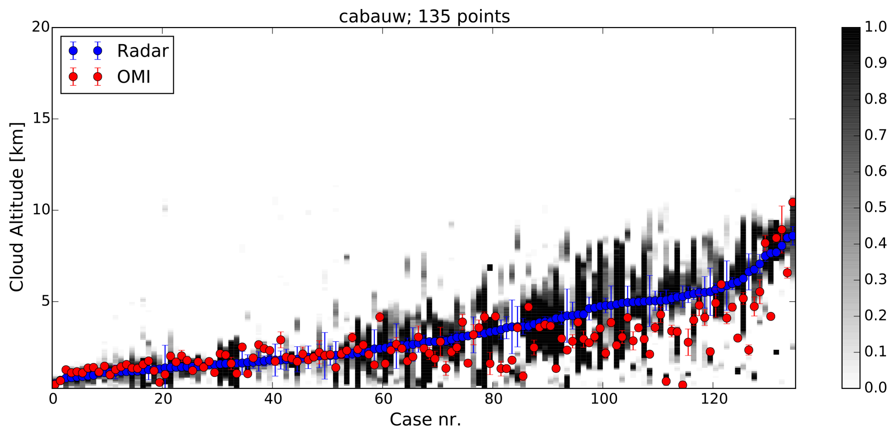

Figure 10: The effective cloud altitude retrieved from OMI (red), compared to radar cloud information for Cabauw (blue), The Netherlands. The grey background is the vertically resolved cloud occurrence derived from the radar data for the period +/- 30 minutes of the OMI overpass. The cases are ordered according to the ground station cloud mid-height.

Atmos. Meas. Tech. Discuss., doi:10.5194/amt-2016-48, 2016
Manuscript under review for journal Atmos. Meas. Tech.
Published: 6 April 2016

Atmospheric Measurement Techniques
Discussions

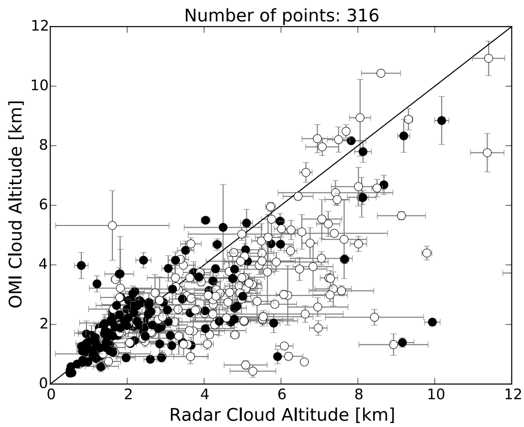

Figure 11: The retrieved effective cloud altitude from OMI, plotted as a function of the radar derived cloud altitude. Closed symbols are for single-layer clouds, open symbols for multi-layer clouds.